Non-hydrostatic modelling with ICON

Almut Gassmann

Max Planck Institute for Meteorology (MPI-M)
Bundesstr. 53, D-20146 Hamburg
Almut.Gassmann@zmaw.de

ABSTRACT

This article gives an overview on the status of the ICON model development currently under way at MPI-M and DWD. It raises the most important issues and model features, but it can not be possible to give a more detailed scientific description in this short overview document.

1   History and motivation

In 2001, DWD (Deutscher Wetterdienst) and MPI-M (Max Planck Institute for Meteorology) started out an initiative for a joint development effort towards a new global circulation model. The main motivation was to bring together the expertise in climate modeling (ECHAM/MPIOM) and numerical weather prediction (GME, COSMO) with the intention for each institution to take advantage of the other's experience. We expect that the processes and scales considered in each community will converge in the future.

Several targets were defined at this time: The model should work in Voronoi-Delaunay gridpoint space generated by the tesselation of an icosahedron. Elaborated tracer transport schemes should conform with the continuity equation. Local grid refinement allows to supersede parts of the model chain in NWP, e. g. the COSMO-EU model part. The possibility to access more parts of the climate system (coupling to ocean) is promising also for NWP applications. Smaller non-hydrostatic scales open a new perspective to investigate the climate system for the MPI-M. Specific properties for the numerics were envisaged: C-grid staggering, conservation of mass, tracer mass, energy, and potential vorticity.

The project accelerated the development speed during the last 3 years, so that within the next year a fully blown prototype model will be available. Currently, work is going on in the development of hydrostatic and non-hydrostatic atmosphere and ocean models and their coupling.

2   Non-hydrostatic equation set and discretisation strategy

Because we use a C-staggered mesh, vorticity and divergence are naturally defined via the Stokes and Gauss integral theorems, which leads us to choose the velocity vector components as prognostic variables. In contrast to that choice, the momentum components as prognostic variables would call for a full finite volume approach and thus a divergence of the momentum flux tensor. But with the vorticity so easily accessible, we can take advantage of the vector invariant form (Lamb's form) of the velocity advection term combined with the Coriolis term

$$\mathbf{v} \cdot \nabla \mathbf{v} + 2\vec{\Omega} \times \mathbf{v} = \nabla K + \vec{\omega}_a / \rho \times \rho \mathbf{v}. \tag{1}$$

Summarizing the velocity equation, we have

$$\frac{\partial \mathbf{v}}{\partial t} = -\frac{\vec{\omega}_a}{\rho} \times \rho \mathbf{v} - \nabla(K + \Phi) - c_{p,d}\theta_v \nabla \Pi + \mathbf{f_r}. \tag{2}$$

If one chooses the continuity equation for total mass ($\rho = \sum_i \rho_i$)

$$\frac{\partial \rho}{\partial t} = -\nabla \cdot (\rho \mathbf{v}) \tag{3}$$

and the equation for the virtual potential temperature

$$\frac{\partial \rho \theta_v}{\partial t} = -\nabla \cdot (\theta_v \, \rho \mathbf{v}) + \rho Q^{(\theta_v)} \tag{4}$$

as prognostic equations, energy conservation has to be guaranteed implicitly by mimicking the properties of a scalar triple product and the product rule of differentiation in space and time. This is nothing else than discretising Poisson brackets and employing energy conserving (symplectic) time integrators (see Gassmann and Herzog, 2008). Under this aegis a general functional $\mathscr{F}$ undergoes an evolution equation written as

$$\frac{\partial \mathscr{F}}{\partial t} = \{\mathscr{F}, \mathscr{H}\} + (\mathscr{F}, \mathbf{f_r}) + (\mathscr{F}, \mathscr{Q}^{(\theta_v)}), \tag{5}$$

where $\mathscr{H}$ is the adiabatic dry limit energy functional (the Hamiltonian) and the last two terms on the rhs signify frictional and diabatic source terms. The first term on the rhs is the Poisson bracket defined as

$$\begin{aligned}
\{\mathscr{F}, \mathscr{H}\} = & -\int_V \frac{\delta \mathscr{F}}{\delta \mathbf{v}} \cdot \left(\frac{\vec{\omega}_a}{\rho} \times \frac{\delta \mathscr{H}}{\delta \mathbf{v}}\right) d\tau \\
& -\int_V \left(\frac{\delta \mathscr{F}}{\delta \rho} \nabla \cdot \frac{\delta \mathscr{H}}{\delta \mathbf{v}} - \frac{\delta \mathscr{H}}{\delta \rho} \nabla \cdot \frac{\delta \mathscr{F}}{\delta \mathbf{v}}\right) d\tau \\
& -\int_V \left(\frac{\delta \mathscr{F}}{\delta \tilde{\theta}_v} \nabla \cdot \left(\theta_v \frac{\delta \mathscr{H}}{\delta \mathbf{v}}\right) - \frac{\delta \mathscr{H}}{\delta \tilde{\theta}_v} \nabla \cdot \left(\theta_v \frac{\delta \mathscr{F}}{\delta \mathbf{v}}\right)\right) d\tau,
\end{aligned} \tag{6}$$

where $\tilde{\theta}_v = \rho \theta_v$. If one discretises this bracket, the integrals turn into sums over grid boxes. To evaluate the bracket one has to define the divergence operator, a reconstruction method for θ_v at grid box interfaces (obtained from an elaborated advection scheme), a vector reconstruction method to evaluate the scalar triple product in the first line of the above bracket, and a rule to achieve the vorticity components. The equations (2-4) follow directly if the functional $\mathscr{F}$ is replaced by (delta functionals of) the prognostic variables encountered at the grid points. Interestingly, the gradient operator does not directly appear in the bracket. As it is the dual operator of the divergence it is automatically generated if needed. This is of advantage, especially if one deals with terrain-following coordinates in which the pressure gradient term is a nuisance.

The symplectic time integrator obeys a similar integration by parts rule to achieve energy conservation as hidden in the 2nd and 3rd line of (6) for the spatial discretisation. A nonlinear quantity AB is conserved if its discrete time integration scheme is written as

$$\frac{A^{n+1}B^{n+1} - A^n B^n}{\Delta t} = A^{n+1}\frac{B^{n+1} - B^n}{\Delta t} + B^n \frac{A^{n+1} - A^n}{\Delta t}. \tag{7}$$

One can show that the well known forward-backward time integration scheme often employed for the horizontal discretisation is compatible with that viewpoint, but the nonlinear advection terms for velocity have to be included via a Runge-Kutta midpoint method. This prohibits the use of time-split methods from the outset. The vertical implicit scheme is also energy conserving if special implicit weights are employed (Gassmann and Herzog, 2008). ICON thus does neither employ global implicit solvers nor time-splitting in the dynamical core. With regard to the future multicore architectures, it does not need
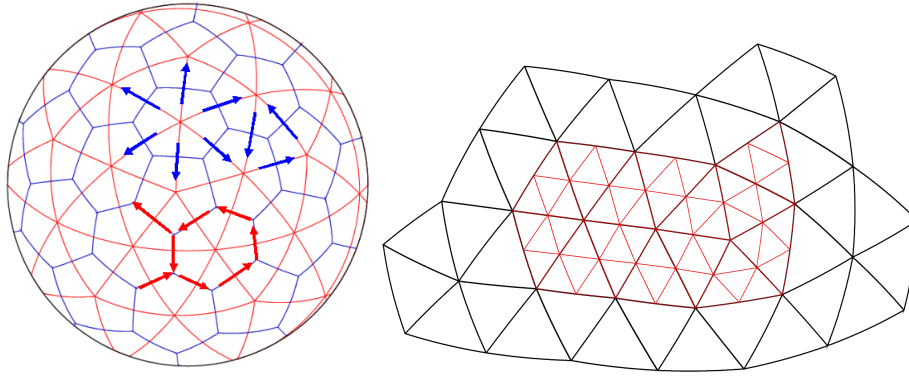
Figure 1: ICON grid. Left: Triangular C-grid configuration in red color, hexagonal C-grid configuration in blue color. Right: For mesh refinement with the triangular C-grid, parent triangles (black) are connected to 4 child triangles (red) on the next finer resolution level.

global communication and is thus more efficient per time step in the communication, but this occurs at the expense of a relatively small time step limited by the Courant number for horizontally propagating sound waves. As the physics routines need generally more resources than the dynamics, both institutions (MPI-M and DWD) work on strategies to reduce the number of calls for physics subroutines and the usage of a so called 'reduced grid' for physics.

A main challenge in defining the non-hydrostatic equation set is to include turbulence and moisture in such a way that the envisaged conservation properties are not violated, and at the same time the equations remain in view of the following discretisation step as simple as possible. In equation (2) the pressure gradient term arrives with the Exner pressure and the virtual potential temperature defined as

$$\Pi = \left(\frac{p}{p_{00}} \right)^{R_d/c_{p,d}} \qquad \theta_v \Pi = T_v,$$

where the exponent does not depend on the moisture content, but solely on the properties of dry air (*d*). This form avoids a pressure gradient correction term which is dependent on moisture quantities entering equation (2) as an explicit add-on. All contributions of moisture in the atmosphere arrive in equation (2) in form of the generalized virtual increment, e. g. $\theta_v = \theta(1+\alpha)$ with $\alpha = (R_v/R_d - 1)q_v - q_l - q_f$, where the specific moisture quantities q_i of water vapour (*v*), liquid droplets (*l*), and frozen particles (*f*) are included with the mass control condition $q_d + q_v + q_l + q_f = 1$. Indirectly, we account thus for the effects of reduced or enhanced buoyancy due to the presence of water in all phases in the atmosphere. Clearly, any q_i has its own tracer mass equation

$$\frac{\partial \rho q_i}{\partial t} = -\nabla \cdot (q_i \, \rho \mathbf{v}) + S_i. \qquad (8)$$

The consistency with the continuity equation for total mass is automatically given, if all species and the total mass are advected with the same mass flux. The 'diabatic' source term $Q^{(\theta_v)}$ in (4) does not only account for diabatic processes like phase changes, but includes also terms that accomplish energy conservation, as for instance the dissipative heating rate and a term which appears as a correction because of the presence of water in all its phases in the atmosphere.

3 C-grid discretisation on triangular and hexagonal C-grids

The ICON model applies C-grid staggered meshes generated from Delaunay-Voronoi tesselations based on the icosahedron. This procedure allows to use both, triangular and hexagonal/pentagonal main grid

boxes as shown in Figure 1 (left). The ICON development started out with the focus on triangles as main boxes (Bonaventura and Ringler, 2005) for two reasons: firstly, the triangular grid seems to be more promising for local grid refinement (Figure 1, right), and secondly, the seminal paper (Thuburn, 2008) for handling dispersion problems on the hexagonal C-grid had not yet appeared. But soon after this breakthrough, we also started with the development of a hexagonal version. Therefore, we now have two versions of the ICON model under development. Both grid types have their own problems, but in some aspects they are related. As they both have the same number of edge degrees of freedom, the representation of a horizontal velocity vector is very similar. An equilateral grid may be described with the help of triavariate coordinate systems with coordinate lines as the red lines in Figure 1. The linearly dependent base vectors are $\mathbf{i_i}$ (parallel to the coordinate lines, suitable for the hexagonal C-grid) or $\mathbf{j_i}$ (perpendicular to the coordinate lines, suitable for the triangular C-grid). A vector in the continuous space can thus be represented in three different ways: either in one of the mentioned trivariate systems or in the common Cartesian frame with base vectors $\mathbf{i}$ and $\mathbf{j}$

$$\mathbf{v} = u\mathbf{i} + v\mathbf{j} = \frac{2}{3}(u_1\mathbf{i_1} + u_2\mathbf{i_2} + u_3\mathbf{i_3}) = \frac{2}{3}(v_1\mathbf{j_1} + v_2\mathbf{j_2} + v_3\mathbf{j_3}). \tag{9}$$

To achieve a unique description of that horizontal velocity vector, the linear dependency among the overspecified trivariate vector components expressed as

$$0 = u_1 + u_2 + u_3 \qquad \text{and} \qquad 0 = v_1 + v_2 + v_3 \tag{10}$$

has to be taken into account. Those expressions must hold in their discretised version, too. Thuburn (2008) showed for the hexagonal C-grid that the obedience to such a linear dependency constraint for the time tendency of the velocity avoids the spurious geostrophic mode which was observed in a previous study of Ničković et al. (2002). It can be shown that if this linear dependency constraint is not fulfilled, a checkerboard pattern will appear in that Stokes/Gauss-integral quantity which is defined on triangles: the vorticity on the hexagonal C-grid, and the divergence on the triangular C-grid. For further reading refer to Gassmann (2010).

For the triangular C-grid, this linear dependency constraint can not be met for the gradient of a scalar like the geopotential in the shallow water equations, because there are too many degrees of freedom in this field. Hence, a checkerboard pattern in divergence is unavoidable. We can only veil the checkerboard by the following measures: averaging of divergence, diffusion of velocity, modification of the discrete specific kinetic energy (from which the gradient is taken). Averaging the divergence can also be interpreted as taking the divergence from rhombus reconstructed normal velocity components. Those measures require a prize to pay: The shortest resolvable gravity or sound wave on this grid has a zero phase speed, which is exactly the property one wants to avoid by the choice of the C-grid staggering. Upper tip and lower tip triangle solutions will decouple for nonlinear problems. Furthermore, in my experience and practice of modeling on the sphere, any attempt for accomplishing energy conservation failed. In other words, it turned out to be impossible to discretise the Poisson bracket (6) and thereby to keep the model stable and without checkerboard pattern in divergence related fields. Among other things, the actual discretisation of the triangular C-grid ICON model does not discretise the full scalar triple product term, it only applies the form (1) in the horizontal and follows the line of COSMO model in the vertical.

For the hexagonal C-grid, the linear dependency constraint can be exactly obeyed in a linear setting on an equilateral grid. Checkerboard pattern in the vorticity on triangles may appear for nonlinear settings or deformed grids. In contrast to the triangular C-grid model, the hexagonal C-grid model can be run stably and without problems with a discretised Poisson bracket (6). A crucial ingredient to fulfill the linear dependency constraint at least approximately on a deformed grid is the definition of the scalar triple product and the velocity reconstruction needed therein (first line of (6)). Its 2-dimensional version is to be found as

$$\{\mathscr{F}, \mathscr{H}\} = -\frac{1}{2} \sum_{hexagons} \frac{\delta \mathscr{F}}{\delta \mathbf{v}} \cdot \left(\mathbf{k} \frac{\omega_a}{\rho} \times \frac{\delta \mathscr{H}}{\delta \mathbf{v}}\right) \Delta A - \frac{1}{6} \sum_{rhombi} \frac{\delta \mathscr{F}}{\delta \mathbf{v}} \cdot \left(\mathbf{k} \frac{\omega_a}{\rho} \times \frac{\delta \mathscr{H}}{\delta \mathbf{v}}\right) \Delta A... \tag{11}$$
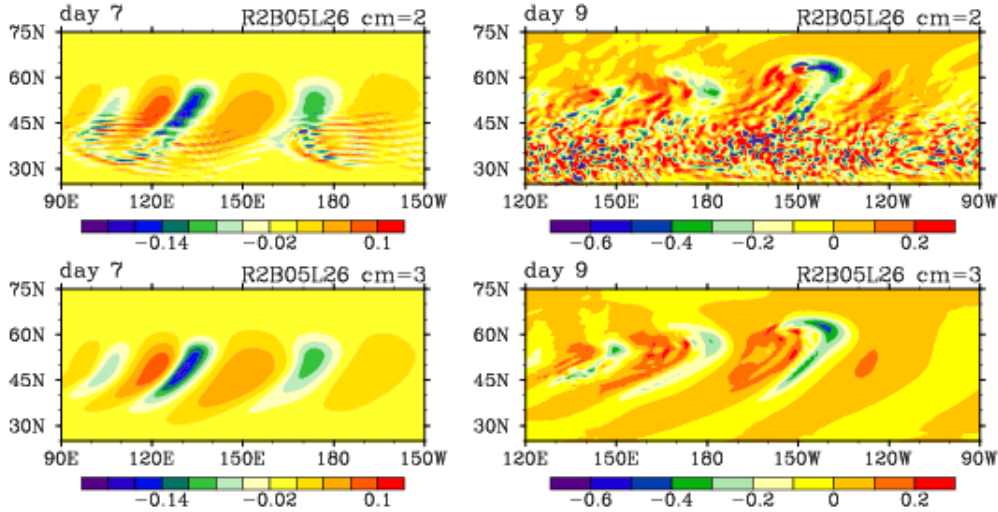
Figure 2: Pressure vertical velocity field (Pa/s) in 850 hPa. Upper row: model version with SICK. Lower row: model version corrected for SICK.

with

$$\frac{\delta \mathscr{F}}{\delta \mathbf{v}}\bigg|_i = \frac{1}{A_i} \sum_{e \in i} \tilde{\delta}_{e,i} \lambda_e \frac{\delta \mathscr{F}}{\delta v_e} \mathbf{N}_e. \tag{12}$$

The *i*-indices refer to hexagons or rhombi, respectively. The λ_e are the edge lengths of those entities, and $\tilde{\delta}_{e,i}$ is the distance between the edge midpoint and the midpoint of the considered entity: the hexagon or the nearest triangle center, respectively. The rhombus reconstruction is in fact a reconstruction using the 6 edges of two neighboring triangles, the center edge of the rhombus is counted twice.

Another issue has to be taken into account on both C-grids: the stencil for the vorticity flux term becomes quite large as a result of the special tangential wind reconstruction method. It is larger than the stencil which is covered by the gradient of the specific kinetic energy. Even the linearised horizontal part numerical equivalence between the lhs and the rhs of equation (1) is not obtained. In this situation, a so called 'symmetric instability of computational kind' (SICK) is likely to appear (Hollingsworth et al., 1983). In the hexagonal hydrostatic ICON model version it is visible as zonal stripes in the divergence field that later break and leave a chaotic small scale flow pattern. Figure 2 (upper row) displays the vertical velocity pattern at days 7 and 9 of the standard baroclinic wave test case (Jablonowski and Williamson, 2006) in case of the hexagonal C-grid run without diffusion on an approximately 120 km horizontal mesh. In the non-hydrostatic ICON model version this instability seems to trigger erroneous behaviour in the vicinity of the pentagons. This instability can be avoided by averaging the kinetic energy in a special way (Figure 2; lower row). In case of the hexagonal C-grid energy conservation can be incorporated easily in that philosophy.

4 Terrain-following coordinates and vertical grid staggering

The ICON non-hydrostatic model uses terrain-following height coordinates and an L-grid vertical staggering. The prognostic velocities are stored as orthogonal values. For the divergence computation, the contravariant velocity components have to be diagnosed to apply them in the Gauss integral theorem. For the vorticity computation, the covariant components have to be diagnosed to apply them in the Stokes integral theorem. Naturally the vorticity components appear as contravariant measures, but for simplicity, the scalar triple product in (6) is computed with orthogonal components. Thus, a further step

is needed that converts the contravariant vorticities into orthogonal ones. The contributions to the kinetic energy are the orthogonal values, a cumbersome alternative not used in ICON would be to multiply covariant and contravariant measure numbers.

The vertical position of the layer centers and interface heights can be defined in two ways. The traditional version which is also used in the COSMO model positions the layer centers half way (in height) inbetween the interface heights. An alternative version puts the interface height half way inbetween the layer center heights. Both approaches are implemented into ICON and are currently under investigation. The second alternative has the advantage of achieving a centered second order accurate vertical pressure gradient term, and allows for the employment of the vector invariant velocity advection form (cf. equation (2)) in three dimensions: Sadourny's (1975) energy conserving form can be applied in a vertical slice, and at the same time a SICK instability can not occur because for a horizontal velocity u one finds

$$\frac{\overline{\Delta \overline{u^2/2}^x}}{\Delta z} = \overline{\overline{u}^z \frac{\Delta u}{\Delta z}}^x .$$
(13)

Here, the lhs is identified as a part of the specific kinetic energy gradient term, and the rhs is equivalently part of the vorticity flux term.

In meteorological modeling, the horizontal pressure gradient term in terrain-following coordinates is often blamed to induce spurious vertical velocity artefacts in an atmosphere initially at rest. Several measures to circumvent this nuisance were discussed in the past: The philosophy of 'well balancing' reconstructs and removes a local hydrostatic background state pressure in every time step. Unfortunately, this is a very costly enterprise, as the reconstruction needs the evaluation of expensive exponential functions in every time step. Another often discussed approach is the use of a z-coordinate, but it is not trivial to formulate boundary conditions, drive it towards efficiency, and include subgrid-scale parameterization schemes. Therefore, we compute the orthogonal horizontal velocity equation directly from the covariant horizontal and vertical velocity equations

$$\frac{\partial u_{orth}}{\partial t} = \frac{\partial u_{cov}}{\partial t} - J_x \overline{\frac{\partial w}{\partial t}}^{zx} ,$$
(14)

where J_x is the slope of the terrain in the horizontal direction. As $\partial w/\partial t$ has a well defined lower boundary (free slip), commonly met problems with a one sided difference in the metric correction term for the pressure gradient do not occur. There is no need to remove a background reference profile for the pressure in the covariant equations. In retrospect it seems that the usual removal of a background state before transforming the equations to the terrain-following coordinates may disrupt the hydrostatic equation part which is present in both covariant equations for itself. Experiments using (14) for a resting atmosphere testcase revealed its capacity. Figure 3 shows the upward air velocity after 12 hours over a
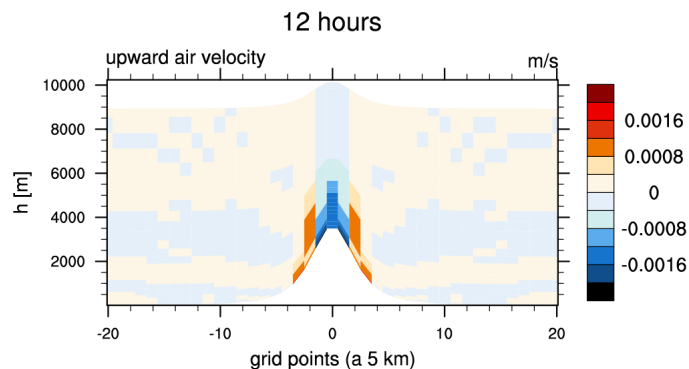

Figure 3: Vertical velocity after 12 hours in the resting atmosphere testcase.

4 km high mountain with a half width of 20 km, horizontal resolution of 5 km, and a stratification with $N^2 = 10^{-4}/s^2$. The spuriously generated vertical velocity remains well in the range of mm/s, which is acceptable. Further experimenting suggests, that instabilities may occur because the second term on the rhs of (14) is treated explicitly in the time integration scheme (it is the forward step of the forward-backward time integration scheme), but the actual w-equation is required to be temporarily implicit.

An alternative method for the horizontal pressure gradient term in terrain-following coordinates is to search for a neighboring point in the same height and then to reconstruct the Exner function at this location using a Taylor expansion until the second order, but this would be inconsistent with the discretisation of the Poisson bracket (6).

5 Tracer advection

As already mentioned, the virtual potential temperature and the specific moisture quantities have to be transported in consistency with the continuity equation. For the triangular and the hexagonal C-grid models different methods are employed, but both use the same polynomial reconstruction method for the subgrid distribution of the tracer variable.

For the triangular C-grid model, the method of Miura (2007) was implemented into ICON by Daniel Reinert (DWD). Its main idea is to define a departure region (see Figure 4, left) and to determine the tracer mass flux that crosses the cell boundary during one time step under the assumption of a constant advection velocity. The tracer distribution inside the departure region is obtained by a Taylor series expansion

$$q^R(\vec{x} - \vec{x}_i) = q|_{\vec{x}_i}^n + \frac{\partial q}{\partial x}\Big|_{\vec{x}_i}^n (x - x_i) + \frac{\partial q}{\partial y}\Big|_{\vec{x}_i}^n (y - y_i) + \frac{1}{2}\frac{\partial^2 q}{\partial x^2}\Big|_{\vec{x}_i}^n (x - x_i)^2 + \frac{1}{2}\frac{\partial^2 q}{\partial y^2}\Big|_{\vec{x}_i}^n (y - y_i)^2 + \frac{\partial^2 q}{\partial x \partial y}\Big|_{\vec{x}_i}^n (x - x_i)(y - y_i)$$

(15)

around the cell center point i. Here, it is given exemplarily up to second order. ICON offers the possibility to choose this expansion to be of first, second, or third order. The coefficients in (15) are obtained by a conservative[1] least squares reconstruction using the values from neighboring cells, as illustrated in Figure 4 (right). A Gauss-Legendre quadrature rule is used to perform the integration over the rhomboidally shaped area sketched in Figure 4 (left). There is still room for improvement of the current implementation by considering that the mentioned area covers several triangles with different subgrid-scale tracer distributions that have to be integrated separately. Figure 5 shows the results for the advected tracer field for the deformational flow testcase described in Nair and Lauritzen (2010) at half and full cycle time of the time-varying flow field. Here, the cubic reconstruction was used for the tracer field.
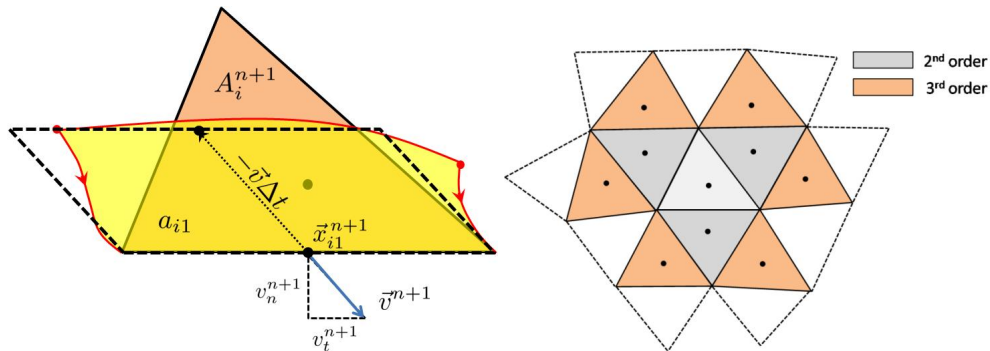
---

[1] only for 2nd and 3rd order expansion

Figure 4: Tracer advection scheme for the triangular C-grid scheme.
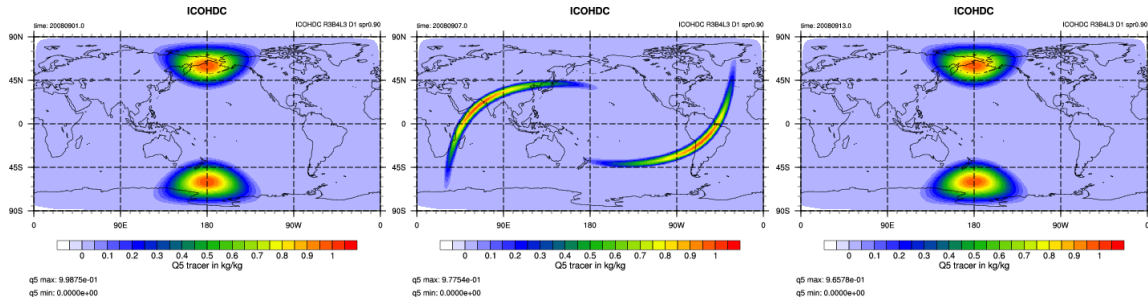
Figure 5: Left: initial tracer field. Center: tracer distribution at half cycle time. Right: tracer distribution at full cycle time.

For the hexagonal C-grid model, the same method is envisaged to be implemented. Currently, only a transport scheme for θ is available that takes advantage from the recognition that higher order advective fluxes can be obtained by correcting a second order tracer interface value with addional terms containing the second derivatives of the tracer (here θ) polynomial

$$\theta_{i+1/2} \quad = \quad \overline{\theta}^{i+1/2} - \frac{\Delta x^2_{i+1/2}}{12}\left(\left.\frac{\partial^2 \theta}{\partial x^2}\right|_{i+1} + \left.\frac{\partial^2 \theta}{\partial x^2}\right|_{i}\right) + \beta \operatorname{sign}(u_{i+1/2}) \frac{\Delta x^2_{i+1/2}}{12}\left(\left.\frac{\partial^2 \theta}{\partial x^2}\right|_{i+1} - \left.\frac{\partial^2 \theta}{\partial x^2}\right|_{i}\right) \quad (16)$$

A 3rd (4rth) order scheme is obtained by setting $\beta = 1(0)$. The requested second derivatives of the tracer polynomials are obtained with the same conservative least squares reconstruction method as developed for the triangular C-grid. Higher order transport can reduce the phase lag of a baroclinic wave on a coarse mesh compared to a simulation on a fine mesh (Skamarock and Gassmann, 2010). Figure 6 displays the phase lag of 2nd, 3rd, and 4th order advection schemes for potential temperature with different coarse resolution runs (240, 120, 60 km) compared to a run with a 30 km mesh. The runs were performed without diffusion for velocity and temperature.

6 Physics parameterizations

One of the main advantages of the ICON project is the synergy effect due to the collaboration of both institutions, DWD and MPI-M. Most of the code for physics parameterization schemes developed inde-
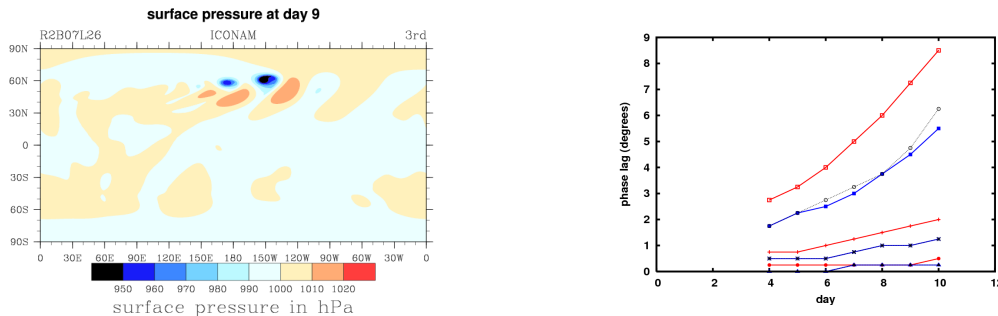

Figure 6: Left: surface pressure field of the baroclinic wave experiment after 9 days on a 30 km mesh. Right: Phase lag of the baroclinic wave development with respect to the finest resolution (30 km); red: 2nd order advection, blue: 3rd order advection, black: 4th order advection; upper 3 lines: 240 km mesh, middle 3 lines: 120 km mesh, lower 3 lines: 60 km mesh.
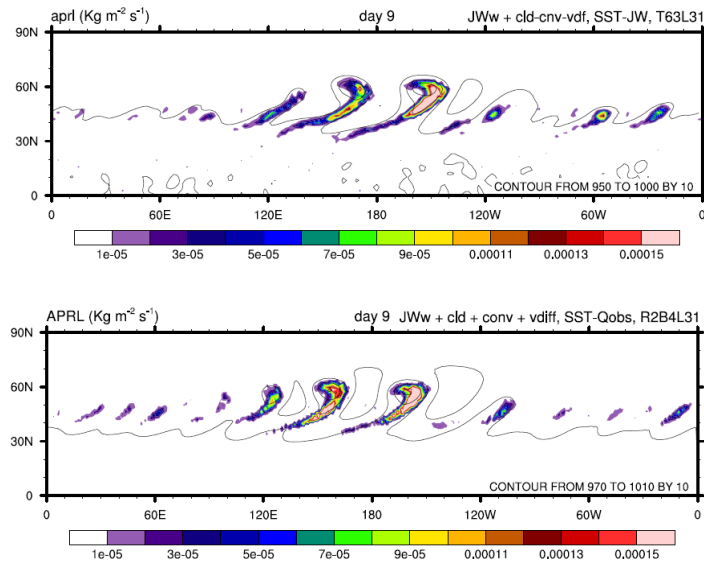
Figure 7: Large scale preciptation in the last 6 hours. Snapshot at day 9 of the moist baroclinic wave test. Upper panel: ECHAM run. Lower panel: ICOHAM triangular C-grid run.

pendently by both institutions is now available for ICON.

For the hydrostatic version of ICON, named ICOHAM (ICOsahedral Hydrostatic Atmospheric Model), which follows the vertical discretisation philosophy of Simmons and Burridge (1981), the parameterisation schemes of the ECHAM model are accessible. In order to apply all of them, the horizontal wind vector has to be reconstructed in geographical vector components at the cell centers. The parameterisation tendencies are first obtained at the cell centers and afterwards the normal wind tendencies are recovered at the edge positions. The following packages are already implemented by Hui Wan (MPI-M) and Marco Giorgetta (MPI-M)

- large scale condensation

- cumulus convection

- vertical turbulent mixing

- radiation

As a first impression of the performance of ICOHAM with physics, Figure 7 compares the large scale precipitation pattern of ECHAM and ICOHAM at day 9 for the moist baroclinic wave test case. In this experiment, radiation was switched off. ICOHAM in its triangular C-grid version was run with a resolution of approximately 140 km (average distance between two triangle centers), the ECHAM run employed the T63 spectral truncation. The obtained pattern are very similar in structure, but one realizes a phase lag of the ICOHAM model. Here, the temperature advection is still of 2nd order accuracy. On coarse resolutions, the lack of accuracy in the derivative computation for a grid point model in contrast to a spectral model where the derivatives are exact is obviously more pronounced. But as shown in the previous section, higher order accurate advection of the temperature variable can alleviate the problem to a certain degree.

For the non-hydrostatic version of ICON, named ICONAM (ICOsahedral Non-hydrostatic Atmospheric Model) the pool of parameterization schemes of the COSMO model is carried over. In contrast to

ICOHAM an additional conversion module is needed that converts the ICONAM-variables Π, ρ, q_i and θ_v into pressure and temperature, which are the base variables in the COSMO model. A number of parameterization schemes are already made available for ICONAM by Kristina Fröhlich (DWD):

- prognostic microphysics

- saturation adjustment

- convection

- radiation

- cloud cover

- turbulent transfer and diffusion (still under implementation)

For the hydrostatic (Wan, 2009) as well for as for the non-hydrostatic models, the longer term behaviour of the dynamical cores were evaluated within the framework of the Held-Suarez-test (Held and Suarez, 1994). ICONAM in its hexagonal and triangular versions was compared by Maria-Pilar Ripodas (DWD). Both models behave reasonably well, and the currently met slight differences are still a matter of investigation.

7 Local grid refinement

The DWD as an operational service is particularly interested in a detailed numerical weather prediction over Europe. Hence, Günther Zängl (DWD) implemented a local nesting facility into the triangular C-grid version of ICON. The generation of the finer grid is achieved by bisecting the coarse (parent) triangle edges. The newly generated edges lead to the generation of 4 finer triangles, the children (see Figure 1, right). The model supports two versions of dealing with such refined areas:

- **Two-way nesting**
  This algorithm starts out with a full time step for the coarse (parent) mesh, including those regions where the refinement takes place in a subsequent step. The second step is concerned with the interpolation of fields and tendencies to the finer mesh at the lateral interface between the coarse and the fine grid. Third, two small time steps are performed on the refined mesh. The algorithm finishes by a feedback from the fine mesh to the coarse mesh. Thereby, the predicted values on the coarse mesh obtained in the first step of the algorithm are overwritten.
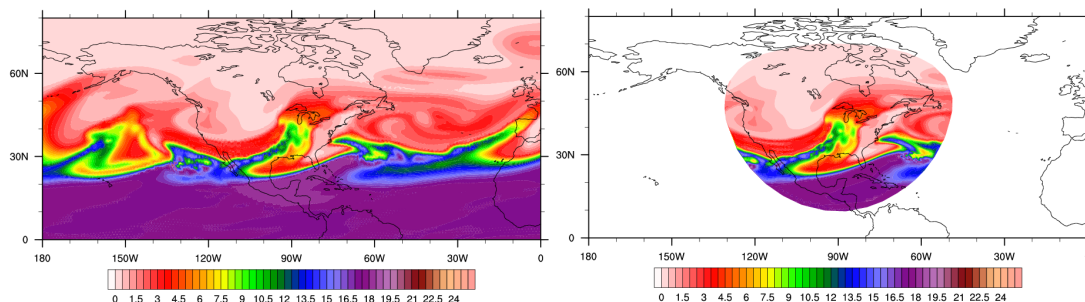

Figure 8: *Specific humidity distribution (g/kg) in 1.8 km altitude. Left: The solution on the coarse mesh (70 km). The information of the fine region is aggregated to the coarse mesh. Right: Only the refined region is plotted on the fine mesh (35 km).*

- **One-way nesting**
  This algorithm differs from the two-way nesting approach only in switching the feedback step off. Additionally, a nudging procedure (Davies, 1976) is applied near the nest boundaries.

Test applications of the two way nesting approach are promising for NWP applications. Figure 8 displays the specific humidity field of a moist baroclinic wave test at day 14 for the coarse and the refined area. At least for that considered field no artefacts are visible that might stem from the transition zone between the coarse and the fine mesh.

8 Efficiency and scalability

The ICON grid structure is special in the sense as it employs an unstructured mesh, where the neighborhood relationships are determined by indirect addressing via tables. Therefore, the cache efficiency is an issue of concern, as there is the danger of cache misses, especially if the address space for neighborhood search is very large. Furthermore, the investments in parallelization and optimization are comparatively large because of the special data structure. Rainer Johanni as an external coworker is developing the parallelization strategy for ICON. For optimization issues, Leonidas Linardakis (MPI-M) is concerned with the compromise of keeping the code as readable as possible for the scientific staff members and of achieving a highly optimized code on various computing architectures, where the model is run. Our different architectures, IBM Power6 at MPI-M (DKRZ) and a NEC-SX-9 at DWD, require different cache optimization strategies. The problem comes to the fore in the speedup diagram displayed in Figure 9. A more than linear speedup is a hint that there are lots of cache misses, especially on coarse resolutions where physically neighboring points may be far away in address space. Hence, there is still room for improvement, e.g. to implement space filling curves. The neighborhood relationships are mainly needed for the dynamical core and to a much lesser extent in the physical parameterizations. Therefore, the overall performance of the model does not suffer too much from those kind of problems.

9 Conclusions and perspectives

This very crude overview could not reveal much detail. I presented only the main features of ICON and did not conceal the problems and trade-offs that appear in such an enterprise. Some of the main goals sketched in the introduction are indeed achieved in our ICON model, among them are tracer-mass-consistency and the local grid refinement. As the hexagonal C-grid version has currently neither grid refinement nor an ocean model under development, and the resources are very limited for those topics, this version will remain a research tool for questions concerning the atmospheric domain.
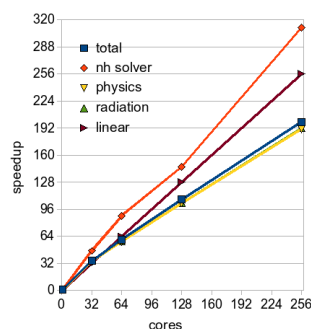

Figure 9: Speedup diagram for the ICONAM model with physics and transport (IBM Power6).

Even though the most serious problems (which arose from the choice of a C-grid discretisation in the trivariate framework) are now controlled, there is still a lot of work in front of us, which mainly requires more collaboration with other groups or departments. To bring forward the operational applicability for NWP at DWD, a data assimilation cycle has to be implemented for ICON. To build a fully blown Earth System Model around ICON at MPI-M requires now to integrate the submodels developed in the Land and Ocean departments of MPI-M.

Whithin the next year we aim at preoperational ICON runs at DWD and a first technically working version of a coupled atmosphere-ocean model at MPI-M.

References

[1] Bonaventura, L. and T. Ringler (2005). Analysis of discrete shallow-water models on geodesic Delauney grids with C-type staggering. *Mon. Weather Rev. 133*, 2351-2373.

[2] Davies, H. C. (1976). A lateral boundary formulation for multi-level prediction models. *Q. J. R. Meteorol. Soc. 102*, 405-418.

[3] Gassmann, A. (2010). Inspection of hexagonal and triangular C-grid discretisations of the shallow water equations. *J. Comput. Phys.*, submitted

[4] Gassmann, A. and H.-J. Herzog (2008). Towards a consistent numerical compressible non-hydrostatic model using generalized Hamiltonian tools. *Q. J. R. Meteorol. Soc. 134*, 1597-1613.

[5] Held I. M. and M. J. Suarez (1994). A proposal for the intercomparison of the dynamical cores of atmospheric general circulation models. *Bull. Amer. Meteorol. Soc. 73*, 1825-1830.

[6] Hollingsworth, A., P. Kallberg, B. Renner, and D. M. Burridge (1983). An internal symmetric computational instability. *Q. J. R. Meteorol. Soc. 109*, 417-428.

[7] Jablonowski, C. and D. L. Williamson (2006). A Baroclinic instability test case for atmospheric model dynamical cores. *Q. J. R. Meteorol. Soc. 132*, 2943-2975.

[8] Miura, H. (2007). An upwind-biased conservative advection scheme for spherical hexagonalpentagonal grids. *Mon. Wea. Rev. 135*, 4038-4044.

[9] Nair, R. D. and P. H. Lauritzen (2010). A class of deformational flow test cases for linear transport problems on the sphere. *J. Comput. Phys.*

[10] Ničković, S., M. B. Gavrilov, and I. A. Tošić (2002). Geostrophic adjustment on hexagonal grids. *Mon. Wea. Rev. 130*, 668-683.

[11] Sadourny, R. (1975). The dynamics of finite-difference models of the shallow-water equations. *J. Atmos. Sci. 32*, 680-689.

[12] Simmons, A. J. and D. M. Burridge (1981). An energy and angular-momentum conserving vertical finite-difference scheme and hybrid vertical coordinates. *Mon. Wea. Rev. 109*, 758-766.

[13] Skamarock, W. C. and A. Gassmann (2010). Conservative transport schemes for spherical geodesic grids: High-order flux operators for ODE-based time integration. *Mon. Wea. Rev.*, submitted

[14] Thuburn, J. (2008). Numerical wave propagation on the hexagonal C-grid. *J. Comput. Phys. 227*, 5836-5858.

[15] Wan, H. (2009). Developing and testing a hydrostatic atmospheric dynamical core on triangular grids. *Reports on Earth System Science, Hamburg*, Ph. D. Thesis.